Optical characterization of the Advanced Virgo gravitational wave detector for the O4 observing run

Optical characterization of the Advanced Virgo gravitational wave detector for the O4 observation run

The Virgo Collaboration: F. Acernese, D. Agarwal, L. Aiello, A. Ain, S. Albanesi, C. Alléné, A. Allocca, A. Amato, C. Amra, M. Andia, M. Andrés-Carcasona, T. Andrade, T. Andrić, S. Ansoldi, S. Antier, E. Z. Appavuravther, F. Armato, N. Arnaud, M. Assiduo, S. Assis de Souza Melo, P. Astone, F. Attadio, F. Aubin, G. Avallone, S. Babak, F. Badaracco, S. Bagnasco, E. Bagui, T. Baka, G. Ballardin, B. Banerjee, P. Barneo, F. Barone, M. Barsuglia, D. Barta, A. Basti, M. Bawaj, M. Bazzan, F. Beirnaert, M. Bejger, D. Belardinelli, L. Bellizzi, I. Bentara, S. Bernuzzi, D. Bersanetti, A. Bertolini, G. Bevilacqua, U. Bhardwaj, V. Biancalana, A. Bianchi, A. Binetti, S. Bini, M. Bitossi, M.-A. Bizouard, F. Bobba, G. Boileau, M. Boldrini, A. Bolliand, L. D. Bonavena, R. Bondarescu, F. Bondu, R. Bonnand, V. Boschi, V. Boudart, A. Boudon, A. Bozzi, C. Bradaschia, M. Branchesi, T. Briant, A. Brillet, M. L. Brozzetti, G. Bruno, F. Bucci, O. Bulashenko, T. Bulik, H. J. Bulten, R. Buscicchio, D. Buskulic, C. Buy, G. Cabras, R. Cabrita, G. Cagnoli, E. Calloni, M. Canepa, G. Caneva Santoro, E. Capocasa, G. Capurri, G. Carapella, F. Carbognani, M. Carpinelli, G. Carullo, J. Casanueva Diaz, C. Casentini, S. Caudill, R. Cavalieri, G. Cella, P. Cerdá-Durán, E. Cesarini, W. Chaibi, E. Chassande-Mottin, S. Chaty, C. Checchia, P. Chessa, F. Chiadini, G. Chiarini, R. Chierici, A. Chincarini, M. L. Chiofalo, A. Chiummo, N. Christensen, G. Ciani, M. Cieślar, P. Ciecielag, M. Cifaldi, R. Ciolfi, S. Clesse, E. Coccia, E. Codazzo, P.-F. Cohadon, S. Colace, A. Colombo, M. Colpi, L. Conti, I. Cordero-Carrión, S. Corezzi, S. Cortese, A. Couineaux, J.-P. Coulon, J.-F. Coupechoux, J. R. Cudell, E. Cuoco, M. Cusinato, B. D'Angelo, S. D'Antonio, L. D'Onofrio, D. D'Urso, G. Dálya, P. Dabadie, S. Dall'Osso, T. Dal Canton, S. Dal Pra, S. Danilishin, V. Dattilo, A. Daumas, N. Davari, M. Davier, P. Davis, J. Degallaix, S. Deléglise, D. Dell'Aquila, F. Della Valle, W. Del Pozzo, G. Demasi, A. Depasse, J. De Bolle, M. De Laurentis, F. De Lillo, F. De Marco, F. De Matteis, R. De Pietri, R. De Rosa, C. De Rossi, R. De Simone, D. Diksha, J. Ding, M. Di Cesare, L. Di Fiore, M. Di Giovanni, T. Di Girolamo, A. Di Michele, S. Di Pace, I. Di Palma, F. Di Renzo, T. Dooney, O. Dorosh, M. Drago, J.-G. Ducoin, U.

Dupletsa, H. Duval, M. Ebersold, H. Einsle, L. Errico, M. Esposito, F. Fabrizi, F. Faedi, V. Fafone, G. Favaro, M. Fays, R. . Felicetti, E. Fenyvesi, T. Fernandes, S. Ferraiuolo, I. Ferrante, F. Fidecaro, P. Figura, A. Fiori, I. Fiori, R. Fittipaldi, V. Fiumara, R. Flaminio, J. A. Font, K. Franceschetti, N. Franchini, S. Frasca, F. Frasconi, A. Frattale Mascioli, A. Freise, O. Freitas, G. G. Fronzé, B. Gadre, S. Galaudage, R. Gamba, B. Garaventa, J. García-Bellido, J. Gargiulo, F. Garufi, C. Gasbarra, F. Gautier, G. Gemme, A. Gennai, V. Gennari, Archisman Ghosh, P. Giri, S. Gkaitatzis, F. Glotin, S. Gomez Lopez, B. Goncharov, M. Gosselin, R. Gouaty, A. Grado, M. Granata, V. Granata, G. Greco, A. C. Green, G. Grignani, C. Grimaud, D. Guerra, D. Guetta, G. M. Guidi, F. Gulminelli, Y. Guo, P. Gupta, N. Gutierrez, M. Haney, S. Harikumar, K. Haris, T. Harmark, J. Harms, B. Haskell, A. Heidmann, H. Heitmann, P. Hello, G. Hemming, S. Hild, S. Hoang, D. Hofman, N. A. Holland, L. Honet, C. A. Hrishikesh, W.-F. Hsu, V. Hui, L. Iampieri, G. A. Iandolo, M. Ianni, A. Ierardi, A. Iess, G. Iorio, P. Iosif, C. Jacquet, P.-E. Jacquet, J. Janquart, K. Janssens, S. Jaraba, P. Jaranowski, V. Juste, I. Khan, W. Kiendrebeogo, G. Koekoek, S. Koley, A. Koushik, A. Królak, S. L. Kranzhoff, J. Kubisz, P. Kuijer, D. Laghi, M. Lalleman, A. Lartaux-Vollard, C. Lazarte, C. Lazzaro, A. La Rana, P. Leaci, A. Lemaître, M. Lenti, M. Leonardi, M. Lequime, N. Leroy, N. Letendre, M. Lethuillier, K. Leyde, M. Le Jean, T. G. F. Li, J.-P. Locquet, L. London, A. Longo, D. Lopez, M. Lopez Portilla, M. Lorenzini, V. Loriette, G. Losurdo, L. Lucchesi, D. Lumaca, A. Macquet, S. Maenaut, R. Maggiore, M. Magnozzi, E. Majorana, N. Man, V. Mangano, M. Mantovani, M. Mapelli, D. Marín Pina, F. Marchesoni, C. Marinelli, F. Marion, S. Marsat, F. Martelli, M. Martinez, V. Martinez, A. Martini, L. Massaro, A. Masserot, M. Mastrodicasa, S. Mastrogiovanni, T. Matcovich, Q. Meijer, S. Mellaerts, L. Mereni, M. Merzougui, B. Mestichelli, A. Miani, C. Michel, A. L. Miller, E. Milotti, V. Milotti, Y. Minenkov, Ll. M. Mir, L. Mirasola, M. Miravet-Tenés, C.-A. Miritescu, A. L. Mitchell, L. Mobilia, C. Mondal, M. Montani, G. Morras, A. Moscatello, B. Mours, C. M. Mow-Lowry, F. Muciaccia, Suvodip Mukherjee, D. Nabari, A. Nagar, D. Nanadoumgar-Lacroze, V. Napolano, I. Nardecchia, H. Narola, L. Naticchioni, G. Nieradka, S. Nissanke, E. Nitoglia, F. Nocera, J. Novak, J. F. Nuño Siles, M. Oertel, A.

Offermans, G. Oganesyan, R. Oliveri, M. Orselli, A. Ouzriat, C. Périgois, L. Paiella, M. A. Palaia, P. P. Palma, C. Palomba, P. Palud, R. Panai, P. T. H. Pang, F. Pannarale, F. Paoletti, A. Paolone, L. Papalini, G. Papigkiotis, A. Paquis, A. Parisi, D. Pascucci, A. Pasqualetti, R. Passaquieti, D. Passuello, B. Patricelli, R. Pegna, A. Perego, G. Perna, A. Perreca, J. Perret, S. Perriès, J. W. Perry, D. Pesios, C. Petrillo, K. S. Phukon, M. Piarulli, L. Piccari, M. Pichot, M. Piendibene, F. Piergiovanni, L. Pierini, G. Pierra, V. Pierro, M. Pietrzak, M. Pillas, F. Pilo, L. Pinard, I. M. Pinto, M. Pinto, A. Placidi, E. Placidi, W. Plastino, R. Poggiani, E. Polini, E. Porcelli, E. K. Porter, R. Poulton, M. Pracchia, T. Pradier, G. Principe, M. Principe, G. A. Prodi, P. Prosperi, P. Prosposito, A. Puecher, M. Punturo, P. Puppo, G. Quéméner, G. Raaijmakers, I. Rainho, A. Ramos-Buades, P. Rapagnani, M. Razzano, M. Recaman Payo, T. Regimbau, L. Rei, A. Renzini, P. Rettegno, B. Revenu, A. S. Rezaei, F. Ricci, M. Ricci, A. Ricciardone, S. Rinaldi, F. Robinet, A. Rocchi, L. Rolland, R. Romano, A. Romero, S. Ronchini, L. Rosa, D. Rosińska, D. Rozza, P. Ruggi, E. Ruiz Morales, P. Saffarieh, T. Sainrat, S. Sajith Menon, O. S. Salafia, L. Salconi, F. Salemi, M. Sallé, S. Salvador, N. Sanchis-Gual, F. Santoliquido, F. Sarandrea, A. Sasli, P. Sassi, B. Sassolas, S. Sayah, V. Scacco, S. Schmidt, K. Schouteden, M. Scialpi, M. Seglar-Arroyo, D. Sentenac, J. W. Seo, V. Sequino, M. Serra, G. Servignat, A. Sevrin, N. S. Shcheblanov, L. Silenzi, A. Singha, V. Sordini, F. Sorrentino, F. Spada, V. Spagnuolo, M. Spera, P. Spinicelli, D. A. Steer, J. Steinlechner, S. Steinlechner, N. Stergioulas, P. Stevens, F. Stolzi, G. Stratta, M. Suchenek, S. Sudhagar, J. Suresh, B. L. Swinkels, A. Syx, M. J. Szczepańczyk, P. Szewczyk, M. Tacca, N. Tamanini, E. N. Tapia San Martín, C. Taranto, A. Theodoropoulos, J. Tissino, P. Tiwari, A. Torres-Forné, M. Toscani, I. Tosta e Melo, E. Tournefier, M. Trad Nery, A. Trapananti, F. Travasso, M. C. Tringali, G. Troian, A. Trovato, L. Trozzo, K. Turbang, M. Turconi, C. Turski, H. Ubach, M. Vacatello, M. Valentini, S. Vallero, N. van Bakel, M. van Beuzekom, M. van Dael, J. F. J. van den Brand, C. Van Den Broeck, M. van der Sluys, A. Van de Walle, J. van Dongen, H. van Haevermaet, J. V. van Heijningen, P. Van Hove, Z. Van Ranst, N. van Remortel, M. Vardaro, G. Vedovato, S. Venikoudis, P. Verdier, M. Vereecken, D. Verkindt, P. Verma, F. Vetrano, A. Veutro, A. Viceré, J.-Y. Vinet, S. Viret, A. Virtuoso, H. Vocca, A. Wajid, M. Was, M. Wils, J. Woehler, N.

YADAV, N. YADAV, A. ZADROŻNY, T. ZELENOVA, J.-P. ZENDRI, M. ZEOLI, M. ZERRAD, Y. ZHAO

Virgo Collaboration
*yuefan.guo@maastrichtuniversity.nl

Abstract: The Advanced Virgo Plus detector, an upgrade of the Advanced Virgo Detector, is a Dual-Recycled Fabry-Perot Michelson Interferometer characterized by 3 km long arm cavities. The main upgrades in view of the fourth Observing Run (O4) were the implementation of the Signal Recycling Cavity and the installation of the Frequency Dependent Squeezing system. Another upgrade was the increasing of the laser power at the input of the detector, which could lead to more severe thermal aberrations impacting the achievement of the interferometer optimal working point. Therefore, also the fine tuning of the Thermal Compensation System, optimized with respect to the one implemented for the O3 run, was also challenging. In order to achieve the best performance of such a sophisticated optical system, having a clear knowledge of all its optical parameters is crucial. The optical characterization of the detector in different working conditions could help in understanding its behavior and optimizing the global control system. Moreover, the characterization in different thermal conditions, i.e. different values of the input laser power or different configuration of the Thermal Compensation System, could provide a significant guidance to the optimization of the thermal tuning. In this paper, we will describe all the methodologies adopted for the optical characterization activities performed in Advanced Virgo Plus, presenting the experimental results for all the relevant parameters obtained in view of the O4 run.

1. Introduction

In 2020, the Advanced LIGO [1] and Advanced Virgo [2] gravitational-wave (GW) detectors officially concluded the third scientific Observing Run (O3) and started an upgrade phase aimed to improve their sensitivity. The upgraded configuration of the Advanced Virgo detector is called Advanced Virgo Plus (AdV+) and the project was conceived to be implemented into two different phases. The phase I, planned to be accomplished for the fourth scientific Observing Run (O4) [3], aimed at reducing the impact of the quantum noise on the sensitivity. This target was planned to be reached thanks to the increase of the input power, the implementation of the Signal Recycling Cavity (SRC) and the installation of the Frequency Dependent Squeezing (FDS) system. The phase II target was initially planned to reduce the impact of the coating thermal noise on the sensitivity. It consisted in the modification of the optical geometry of the arm cavities, increasing the size of the optical laser beam impinging on the end test masses, that implies the installation of larger mirrors (in conjunction with a coating with potentially lower mechanical loss) [4]. The target is to conclude the phase II installation before the fifth scientific Observing Run (O5) [5]. However, due to issues discovered during the phase I commissioning, the plan for phase II has shifted toward increasing the robustness of the recycling cavities. Since Initial Virgo, the recycling cavities of Virgo are marginally stable with no focusing element in those cavities, similar to flat-flat cavities whose g-factor are close to 1, at the limit of the stability. Such configuration, limiting the number of mirrors, fits well in the infrastructure with constraint space. However, it is extremely sensitive to optical aberrations. So during the years 2023-2024, it was decided to install stable recycling cavities in Virgo before O5, so the current goal of phase II is now a large infrastructure change in the central part of the interferometer rather than installing large end test masses.

During the commissioning, to optimize the working point of the instrument, fundamental information should be deduced by performing measurements of its optical performance. A comprehensive optical characterization of a gravitational-wave interferometer includes the analysis of the Fabry-Pérot arm cavity, power recycling cavity, and dark fringe. The methods and results of these characterization will be discussed in Sections 3 and 4, respectively, following a detailed overview of the Advanced Virgo Plus detector for the O4 run in Section 2. To fully understand the performance of the interferometer, key parameters such as the length, the mode-matching, the finesse and the round-trip loss (RTL) of the Fabry-Pérot arm cavities, and the estimation of the Radius of Curvature (RoC) of the various test masses were measured through characterization of the arm cavities; the carrier and sidebands recycling gain, the arm circulating power and the power recycling cavity lengths were deduced from the characterization of the power recycling cavity and the contrast defect of the interferometer is calculated while the interferometer is under dark fringe condition. In this paper we describe the techniques used to perform the measurements of the various optical properties of Advanced Virgo and we present the obtained results during the commissioning phase in view of O4.

2. Advanced Virgo configuration for O4

2.1. Dual-recycled Fabry-Perot Michelson Interferometer

A sketch of the optical configuration of AdV+ phase I is shown in Figure 1: it is a Dual-Recycled, Fabry-Pérot, Michelson Interferometer (DRFPMI), working with a laser beam at a wavelength of 1064 nm.

In this configuration, seven main optics are installed: a beam-splitter (BS), a power recycling mirror (PRM), a signal recycling mirror (SRM), an input mirror and an end mirror (WI and WE, respectively) for the arm West arm cavity (WA) and an input mirror and an end mirror (NI and NE, respectively) for the North arm cavity (NA). WA and NA are Fabry-Pérot (FP) cavities used to increase the effective arm length of the Michelson interferometer. The working point of the interferometer is tuned to have a destructive interference for the beams reflected by the arm cavities, the so-called dark fringe (DF) configuration. Therefore, most of the light is reflected back towards the laser source and lost. However, by installing a semi-reflective mirror (PRM) between the BS and the main laser, one can recycle this light and inject it back into the interferometer [6]. The PRM and the two input mirrors form a power recycling cavity (PRC), that allows to increase the effective power circulating inside the detector. The passage of a gravitational wave causes a differential change in the arm length, inducing a phase-shift of the recombined laser beam at the output port. Measuring this out-of-phase beam leaks at the output port leads to the detection of GWs. The installation of a semi-reflective mirror (SRM) between the BS and the output port of the detector allows to shape and optimize the detector frequency bandwidth for specific GW sources. The SRM and the input mirrors form a signal recycling cavity (SRC). Therefore, considering all the main mirrors, there are five longitudinal degrees of freedom that must be controlled:

- **DARM** = $\frac{L_N - L_W}{2}$: **D**ifferential **ARM** length of the two Fabry-Pérot cavities in the arms.
- **CARM** = $\frac{L_N + L_W}{2}$: **C**ommon **ARM** length, average of the lengths of the Fabry-Pérot cavities.
- **MICH** = $l_N - l_W$: Difference between the lengths from the BS and, respectively, the NI and the WI mirrors, forming the **MICH**elson interferometer.
- **PRCL** = $l_{PR} + \frac{l_N + l_W}{2}$: **P**ower **R**ecycling **C**avity **L**ength.
- **SRCL** = $l_{SR} + \frac{l_N + l_W}{2}$: **S**ignal **R**ecycling **C**avity **L**ength.

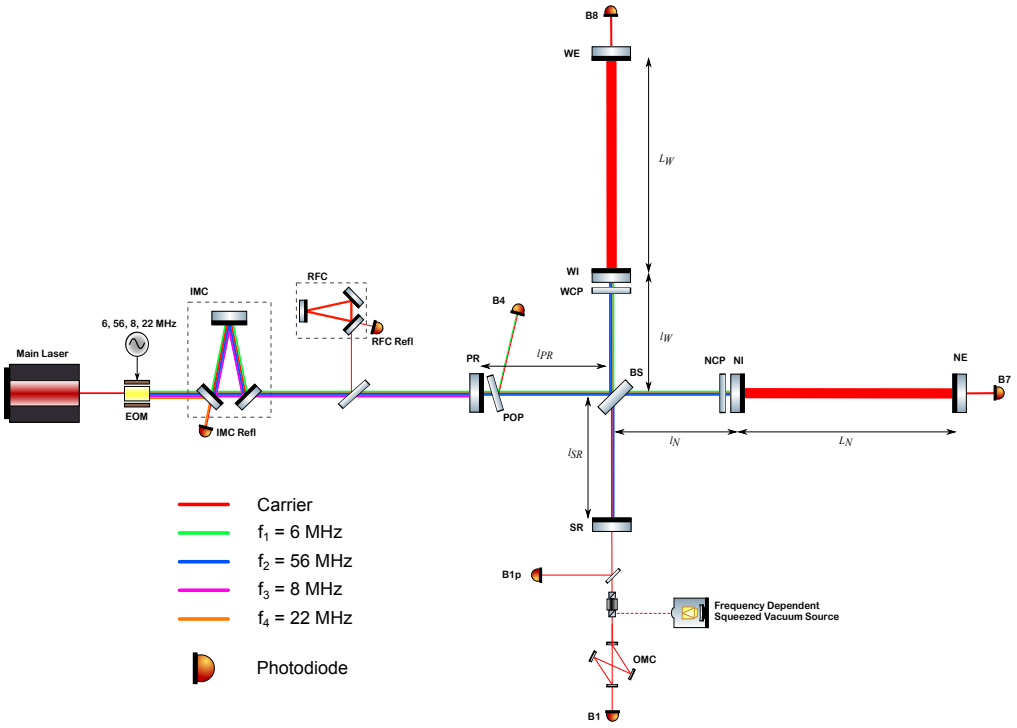

Fig. 1. Advanced Virgo Plus optical configuration for the O4 observing run. The laser beam travels towards the interferometer. It passes through the IMC cavity and the PR mirror, then the laser beam is split at the BS and directed towards the North and West arms. Then, the beams are reflected by the end mirrors of each arm and directed back to the BS, where the beams are recombined and split again towards the input port and the output port passing through the SR mirror. The carrier is shown in red. The different sidebands f_1, f_2, f_3, f_4 are indicated in green, blue, pink and orange respectively. L_{N}, L_{W}, l_{PR} and l_{SR} represents the length of the North arm cavity, West arm cavity, power recycling cavity and signal recycling cavity.

The two recycling cavities and the BS form the so-called central interferometer, including the MICH, PRCL and SRCL degrees of freedom.

Other systems and relevant devices are installed in Advanced Virgo and shown in Figure 1: among them, a high-power stabilized laser, few electro-optic modulators (EOMs), some photodiodes (PDs) and auxiliary optical systems and cavities, such as the Input Mode Cleaner cavity (IMC). The main laser is pre-stablized and phase modulated at different frequencies, $f_1 = 6\,\mathrm{MHz}$, $f_2 = 56\,\mathrm{MHz}$, $f_3 = 8\,\mathrm{MHz}$ and $f_4 = 22\,\mathrm{MHz}$, in order to provide the Pound-Drever-Hall (PDH) [7] control signals for all the degrees of freedom of the whole experiment. The 6 MHz sidebands are resonant inside the power recycling cavity, and anti-resonant inside the arm and signal recycling cavities, the 56 MHz sidebands are resonant inside both the power and signal recycling cavities, but anti-resonant in the arm cavities, the 8 MHz sidebands are anti-resonat and, threfore, fully reflected by the interferometer and the 22 MHz sidebands, reflected by the IMC, are used to control the IMC length. The input mode cleaner cavity filters out higher-order modes, in order to have only the fundamental Gaussian mode entering into the interferometer. Beam jitter and high-frequency noises are both suppressed as well. A reference cavity (RFC), in combination with the IMC, is used to further stabilize the frequency of the main laser. A pick-off of the beam circulating in the power recycling cavity is extracted just after the PRM through a

Pick-Off-Plate (POP) and acquired by a photodiode, named B4. The beams transmitted by the two arm cavities are collected by photodiodes and cameras installed on auxiliary benches. They are called B7 and B8, respectively for the NA and the WA. Two anti-reflective compensation plates (NCP and WCP, respectively for the NI and WI) are located in front of each input test mass, to be shined with the light of CO_2 auxiliary lasers used for the compensation of the thermal aberrations induced by the high circulating power. The beams reflected back from the arms are recombined on the beam splitter. The interference signal passes through the SR mirror and the Outpout Mode Cleaner cavity (OMC) before arriving on the output detectors, named B1. A pick-off of the output beam is extracted before entering the OMC cavity and is acquired by the B1p sensors.
The optical properties of the main test masses, as measured at the Laboratorie des Matériaux Avancés (LMA) [8] are shown in Table 1.

Table 1. Optical parameters of the main test masses individually measured at LMA before the installation in the detector. T (HR) is the power transmissivity of the Highly Reflective (HR) side of the mirror. R (AR) is the power reflectivity of the Anti-Reflective (AR) side of the mirror. RoC (HR) is the radius of curvature of the mirror on the HR side.

Parameters	**NI**	**NE**	**WI**	**WE**	**PRM**	**SRM**
T (HR)	1.377%	4.4 ppm	1.375%	4.3 ppm	4.835%	39.6%
R (AR)	32 ppm	133 ppm	58 ppm	155 ppm	160 ppm	151 ppm
RoC (HR)	1425 m	1695 m	1425 m	1696 m	1477 m	1443 m

Starting from the third Observing Run, the laser input power has been increased from about 10 W to 26 W, to reduce the impact of the shot noise in the high-frequency band. Higher circulating power inside the detector also leads to more power absorbed in the substrate and coating of the mirrors, inducing different optical aberrations. The thermal lensing increases the optical path length in the substrates of the mirrors and the thermo-elastic deformation induces a detuning of the Radius of Curvature (RoC) of the mirrors. These effects could shift the resonances of the recycling cavity higher-order modes (HOMs), creating a degeneracy with the fundamental mode and, consequentially, inducing an offset in the control signals, directly degrading the performance of the detector. A Thermal Compensation System (TCS) [9] was implemented to correct the optical aberrations and find the optimal optical working pointing of the detector.
The TCS consists of sensors and actuators. In particular, the sensors are the Hartmann wavefront sensors [10] used to directly measure the wavefront aberrations, and the phase cameras, which are installed near the B4 and B1p photodiodes and are used to study the carrier and the sideband beams circulating into the recycling cavities. The actuators are the CO_2 projectors and the ring heaters [11], used to induce on purpose a gradient of temperature in the optics to compensate for the aberrations. The ring heaters, which are installed around the mirrors of the Fabry-Pérot cavities, PRM and SRM, could reduce the radius of curvature of each mirror up to 100 m. The CO_2 lasers are installed on two auxiliary benches close to the input mirrors. Their beams are projected on the CPs and not directly on the mirrors, due to their residual intensity fluctuations that could inject displacement noise into the interferometer, degrading the sensitivity. The wavelength of the CO_2 lasers is about 10.6 μm, which is chosen since it is totally absorbed by the fused silica substrate of the CPs. The CO_2 laser could generate different projection patterns: a central heating (CH) beam whose shape is Gaussian, and a double ring produced by a double axicon system (DAS). The rings produced by the DAS are used to compensate for the thermal lensing effect inside the input mirrors. On the other hand, when the interferometer is not locked,

with a small amount of light inside, the beams produced by the CH are used to mimic the thermal lensing effect introduced by the main laser beam to keep a constant thermal state. The different TCS actuators are employed to tune specific parameters of the interferometer. The NE and WE ring heaters can adjust the g-factor of the arm cavities and help to move away the resonance of the fundamental mode to the resonances of the 8th and 9th higher-order modes, reducing cavity optical losses. The differential adjustment of these same ring heaters optimizes the interferometer's contrast defect by making the two arms more symmetric. Additionally, tuning the CH and DAS improves the recycling gains and corrects the imbalance between the lower and upper sidebands by reducing the thermal aberration in the recycling cavities. For the PRM and SRM, other actuators, the Central Heating Radius of Curvature Correction (CHRoCC) systems were implemented [12]. These actuators consist of black-body emitters projecting a circular pattern either on the POP installed close to the PRM or directly on the SRM, which can reduce the radius of curvature of the mirrors. In the final configuration for O4, the CHRoCC actuation is applied on the PRM, while the ring heater is switched on the SRM. Both actuators were tuned in their optimal working points.

One of the most important upgrade of the AdV+ phase I is the implementation of the SRC. As mentioned above, the installation of the SRM introduces a new degree of freedom (SRCL) that should be controlled. Therefore, a new control strategy has been implemented. This requires the installation of an Auxiliary Laser System (ALS) [13]. The ALS is composed of three phase-locked laser beams at 532 nm, generated by doubling the frequency of a pick-off beam of the Virgo main laser [14]: one is implemented near the Virgo main laser and two at the end of the WA and NA, respectively. The two latter beams at 532 nm are then injected with orthogonal polarizations from the end mirrors of the Fabry-Pérot arm cavities. Interfering them with the third beam allows to build the error signals to control DARM and CARM. It is used to arbitrary control the resonance condition of the two arm cavities, while acquiring the control of the central interferometer. During this process, the arm cavities are brought out of resonance for the infrared beam adding an offset on the CARM control loop. By changing this offset, we are able to perform relatively slow scans of a few Free Spectral Range (FSR) of the Fabry-Pérot cavities for the infrared beam.

2.2. Different working conditions

2.2.1. Different input power

In order to find the optimal working point of the detector with respect to the noise for the Observing Run O4, the interferometer has been tested and characterized using different input powers. In particular, input powers of P = 11 W, P = 17 W, P = 22 W, P = 31 W have been injected into the interferometer. The final input power used for the Observing Run O4 is 17 W. Different input powers imply different circulating powers in the detector and, therefore, different tunings of the TCS actuators.

2.2.2. Different TCS tuning

To minimise the noise coupling and the contrast defect, while optimizing the working point of the interferometer, in terms of both stability and performance, different tunings of the TCS actuators have been tested. More specifically, the EM heating ring are used to fine tuned the geometry of the arm cavities to prevent the resonances of the carrier fundamental mode at the same time as some higher order modes (modes of order 8 and 9 are worrisome). A small differential tuning of the rings can also help to improve the symmetry of the cavities amd so reduce the power on the dark fringe. The DAS and CH actions are for the recycling cavities, where they compensate the thermal effects (dominated by the aberrations in the IMs) and helps to maximise the recycling gains and to reduce sidebands imbalance.

Moreover, also measurements have been done with these different tunings to better characterize the detector. For example, when the ring heaters on the end test masses were switched on with the same set points as during O3, we observed a clear change in the spacing among the resonance modes in the arm cavities with respect to the condition with the ring heaters off. Moreover, this change was different between the NA and WA. Furthermore, asymmetrical changes in the optical properties of the two arms have been observed also switching on the CH and DAS actuators.

2.2.3. Different SRM alignment

During commissioning, it was discovered that misaligning the signal recycling mirror could improve the contrast defects of the interferometer. By construction, a marginally stable SRC tuned to enlarge the bandwidth of the detector, brings all the higher order modes on resonance within the cavity. So to reduce the gain of the higher order modes, the signal recycled mirror is on purpose misaligned at the price of higher loss for the fundamental mode. Measurements reported in this paper include both ITF configurations with SRM aligned and with SRM misaligned

2.2.4. Hot and cold cavity

When the interferometer is fully and stably controlled in its final working point, high circulating power inside the Fabry-Pérot cavities leads to a temperature increase in the mirrors due to the absorption in their coatings and substrates. This non-uniform increase of temperature induces wavefront distortions, due to thermorefractive and thermoelastic effects. When the interferometer is stably controlled with the maximum recycling gain, the arm cavities are in a state referred to as 'hot cavities'. On the other hand, at the beginning of the lock acquisition procedure, the amount of power circulating in the arm cavities is low since the power recycling mirror is misaligned. This state is referred to the 'cold cavities' configuration. In order to perform a complete characterization of the detector, optical properties are measured in both configurations. Ideally, measurements done as soon as the interferometer loses the control could represent the 'hot cavities' state. However, after the unlock happens, at least 3 to 4 minutes are needed to recover the status of the detector that allows to perform any measurement, inducing a not negligible decrease in the magnitude of the thermal effects.

3. Optical parameter characterization methods

The optical characterization of the AdV+ detector was carried out during the whole commissioning period towards the Observing Run O4. We give an overview of all the methods used to characterize the optical properties of the different cavities of the detector. In particular, we focus on the characterization of two main parts of the interferometer: the Fabry-Pérot arm cavities and the recycling cavities.

3.1. Arm cavities

For the characterization of the arm cavities, we present two different groups of measurements: Free Spectral Range scans and round trip loss measurements. The FSR scans can be performed in two different ways, the free swing of one of the cavity mirrors or the slow scan of the frequency of the auxilary laser beam. The method used to measure the round trip loss is a comparison between the power reflected by the cavity when it is locked and unlocked.

3.1.1. Free Spectral Range scan

From the scans of Free Spectral Range, different parameters can be extracted, such as: the length difference between two Fabry-Pérot cavities, the mode matching of the input beam into one cavity, the Radius of Curvature (RoC) of the arm cavity mirrors from the cavity g factor and the finesse of the cavity. In Figure 2, a typical FSR of the Virgo arm cavities is shown and it is used

to demonstrate the methods of estimating the optical parameters. Performing a scan of an FSR, we can excite all the resonant modes of the cavity, in particular, the TEM00 and the HOMs of the carrier and sideband beams, as highlighted in Figure 2. From Figure 2, we could get the height

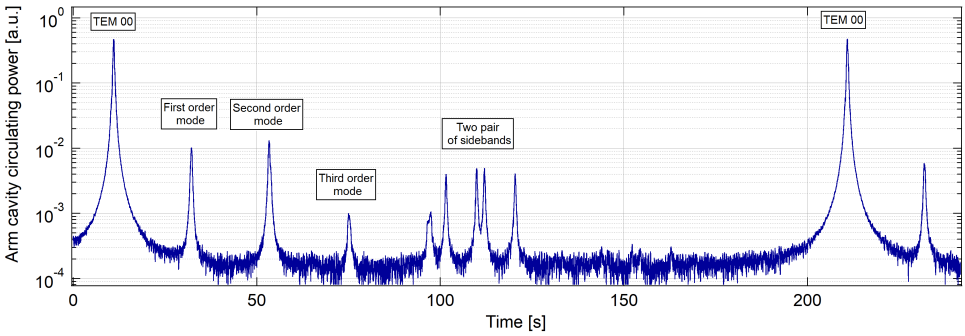

Fig. 2. FSR scan of one Fabry-Pérot arm cavity of the AdV+ detector with the fundamental and high-order modes of the carrier and the fundamental modes of the sidebands labeled.

of each peak and the distance between peaks. In order to estimate precise values of peak heights and distances, we use the Gaussian approximation of the Airy function to fit each peak:

$$I(x) = \frac{a}{1 + \mathcal{F} \cdot \sin^2 \frac{\pi (x - x_0)}{f_{\mathrm{FSR}}}} + o \tag{1}$$

where I(x) is the intensity of the peak as a function of frequency, due to the constant speed of the scan, the x axis can be easily converted from time to frequency, $\mathcal{F}$ is the finesse, a is the amplitude of the peak, x_0 is the expectation value of the distribution and o is an offset. $f_{\mathrm{FSR}} = \frac{c}{2L}$, where c is the speed of light and L is arm cavity length, is the Free Spectral Range, i.e. the distance between two consecutive peaks of the TEM00 mode. All the peaks are normalized to the height of the TEM00 mode and all the distances between peaks are normalized to the FSR.

Before the implementation of the Auxiliary Laser System, the FSR scan was acquired from the free swing of the end mirror of the cavity. In order to induce a larger swing, the mirror is usually excited by the actuators, while the dampers, used to damp the mirror motion, are switched off. Defining τ_{sto} the storage (or decay) time of a cavity, which quantifies how long a photon can stay inside the cavity before it is absorbed or transmitted, when the time needed for the cavity to cross the resonance is shorter than τ_{sto}, the peaks of the modes are distorted by the so-called ringing effect [15]. An example of a distorted resonance peak with the ringing is shown in Figure 3. In this condition, the light does not have enough time to completely fill the cavity and the beat between the incoming field and the evolving field stored in the cavity creates an oscillating pattern, which is called the ringing. As a consequence, a precise measurement of finesse cannot be done using a simple Airy function. However, it's still possible to estimate the storage time by modelling the fields affected by the ringing as [16]:

$$E(t) = D(t)\Theta(t) \tag{2}$$

where:

$$\begin{aligned} D(t) &= \left(\frac{i\pi}{\alpha}\right)^{\frac{1}{2}} t_1 A e^{-\frac{i\beta^2}{\alpha}} \\ \Theta(t) &= \left(\frac{\alpha}{i\pi}\right)^{\frac{1}{2}} \sum_{n=0}^{\infty} e^{i\alpha(n-\beta\alpha)^2} \end{aligned} \tag{3}$$

and:

$$\alpha = \frac{2\pi v}{\lambda f_{\mathrm{FSR}}}$$
$$\beta = \frac{2\pi}{\lambda} vt - i\frac{L}{c\tau_{sto}} \tag{4}$$

where λ is the wavelength of the laser beam, v is the speed of the mirror, and n is the number of round trips. Then the Finesse can be estimated using the storage time:

$$\mathcal{F} = \pi \cdot f_{\mathrm{FSR}} \cdot \tau_{\mathrm{sto}} \tag{5}$$

In Figure 3, the red dots present the fit of the ringing using the above mentioned equations.

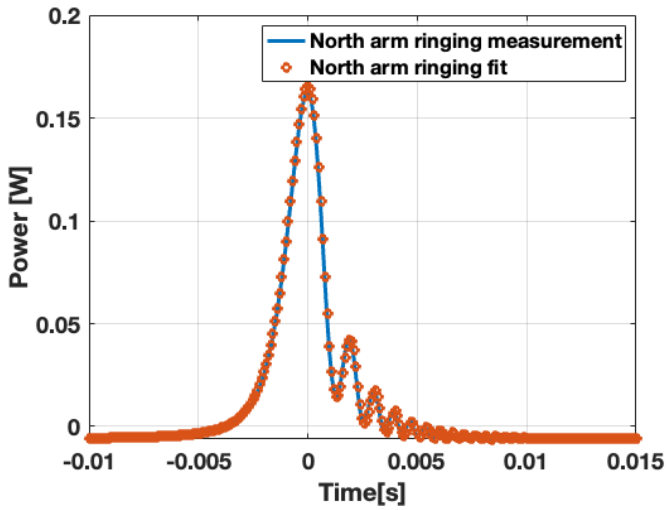

Fig. 3. Resonance peak of one of the AdV+ arm cavities distorted by the ringing effect.

The ALS implemented during the upgrade period after the Observing Run O3 provides a more controllable way to perform scans of the FSR. The ALS allows to lock the arm cavities using a beams at 532 nm, for which the finesse is lower than the one for the infrared beam. The first step to perform the scan is to move the control of the arm cavities from the infrared to the green beam. Using the infrared beam, the arm cavities are controlled and kept at the same length (DARM = 0) by adjusting the mirror positions. Two Acousto-Optic Modulators (AOMs) are installed on the two green beam paths before entering the cavities to control the green frequency. Acting on these AOMs, the green frequency is shifted in order to have the green beam resonant inside the cavities. Beating the green beam generated in the central area with the two transmitted by the cavities, two new signals are produced and combined to form the green CARM and DARM error signals, used to control the cavities instead of the infrared ones. After the lock using the 532 nm beam is acquired, the frequency of the beam is varied at a constant speed in order to scan several FSRs of the infrared beam. To perform slow scans, a gradual change on the offset of the CARM loop is applied, acting on the input mirror positions. The cavity is kept on resonance for the green beam acting on the AOMs. In this way, we can get a more precise measure of the height and the position of the peaks of the fundamental mode, higher-order modes and sidebands.

Cavity length

The Fabry-Pérot arm cavity length can be estiamted through the sideband positions in the FSR scan. From Figure 4, the sidebands f_2 = 56 MHz of the WA and NA have a clear shift between them. It is a zoom of the full free spectral range around the sidebands when the TEM00

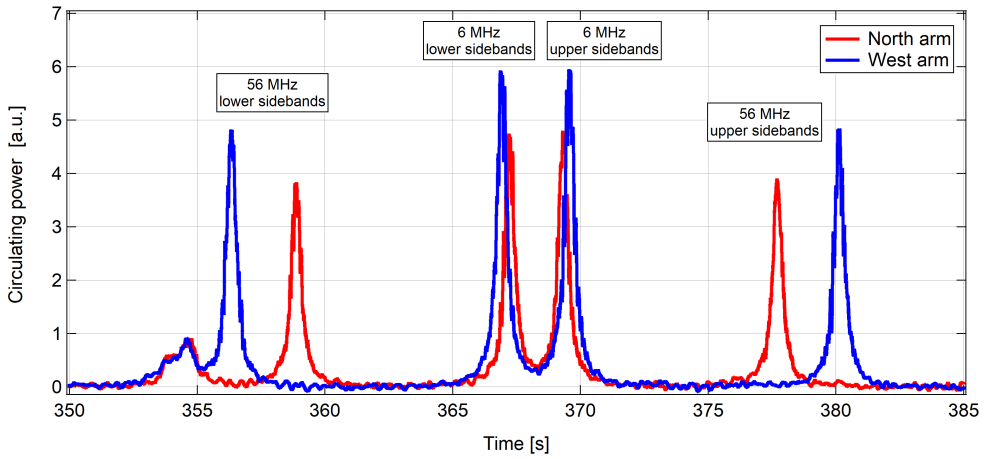

Fig. 4. FSR scan of the North (red) and West (blue) arms of the AdV+ detector zoomed on the 56 MHz and 6 MHz sidebands.

peaks of the carrier are superposed. The scan was repeated multiple times and the results were consistent. This shift in the resonance of the sidebands is due to a small difference in the arm length between the two cavities. Since the cavity length is also crucial for the calculation of other optical parameters, we estimated their values from the following equation:

$$f_{\mathrm{SB}} = N \times f_{\mathrm{FSR}} + d_{\mathrm{SB}} \times f_{\mathrm{FSR}} \tag{6}$$

where f_{SB} is the frequency of the 56 MHz sidebands, N is an integer number and d_{SB} is the normalized distance between the 56 MHz sideband peak and the TEM00 carrier peak. **Mode-Matching**

Comparing the amplitude between the TEM00 and the higher-order modes in the FSR scan, we can extract information for characterizing the arm cavities. Especially, the misalignment and mismatching of the beam can be estimated, since both of them couple the fundamental mode into higher-order modes. The presence of higher-order modes indicates imperfections in the optical system which lead to a decrease in the circulating power and offsets in the error signals, worsening the performance of the interferometer. Therefore, the mismatching and misalignment are crucial information for the control of the interferometer. While improving the mode-matching of the beam into the cavity is related to the fine tuning of the input telescope, reducing the residual misalignment needs to consider the alignment control strategy, that is beyond the work of optical characterization. However, from the scan, information to quantify the misalignment could be extracted. It is given by the comparison between the peak height of the first order Hermite Gauss mode and the fundamental mode. In this paper, our work was mainly focus on the mismatch estimation.

Using the polar coordinates, the amplitude of the fundamental eigenmode of one cavity can be written as [17]:

$$V_0(r) = \sqrt{\frac{2}{\pi}} \frac{1}{\omega_0} \exp\left(-\frac{r^2}{\omega_0^2}\right) \tag{7}$$

where ω_0 is the beam waist size. The field at the input of a cavity can be defined as $\Psi(r) = AV_0(r)$, where A is the amplitude coefficient. The higher-order modes can be written as the generalized Laguerre polynomials L_l^p weighted by a Gaussian function, where p and l are the radial and angular mode numbers. The mode order is defined as $k = 2p + l$. Since the angular dependence is

negligible for our purpose, we set $l = 0$. The amplitude of the first order radial Laguerre-Gaussian (LG) mode, where $p = 1$ and $l = 0$, can be written as:

$$V_{10}(r) = \sqrt{\frac{2}{\pi}} \frac{1}{\omega_0} \left(1 - \frac{2r^2}{\omega_0^2}\right) \exp\left(-\frac{r^2}{\omega_0^2}\right) \tag{8}$$

Considering a mismatch caused by a small difference ϵ between the waist size of the input beam and the one of the cavity, we can define a new beam waist size ω_0' as:

$$\omega_0' = \omega_0(1 + \epsilon) \tag{9}$$

Thus, the input field $\Psi(r)$ becomes:

$$\Psi(r) = A\sqrt{\frac{2}{\pi}} \frac{1}{\omega_0}(1 + \epsilon)\exp\left[-\frac{r^2}{\omega_0^2}(1 + \epsilon)^2\right] \tag{10}$$

Since $\epsilon \ll \omega_0$, the exponential can be expanded and considered only up to the first order of ϵ, resulting in:

$$\Psi(r) \simeq A[V_0(r) + \epsilon V_{10}(r)] \tag{11}$$

which means that a small deviation of the beam waist size will couple the power from the fundamental mode to the second order LG_{10} mode. A similar result could be obtained considering the mismatch caused by a small difference in the position of the waist. Therefore, the level of mismatching is estimated from the comparison between the peak height of the second order mode and the one of the fundamental mode.

Radius of Curvature

The Radius of Curvature of the arm cavity mirrors is another parameter that has been regularly measured during the commissioning period, when the TCS actuators were constantly tuned to find the optimal working point of the interferometer. A precise measurement of the RoCs could also be used in the tuning of the simulations for a better interpretation of the detector behaviour. An estimation of the RoCs can be done starting from the resonance frequency of the different peaks excited performing the scan of the cavity.

The different spatial modes have different resonant frequencies inside the cavity due to their different round trip Gouy phase. The frequency difference between the TEM_{00} mode and the order k mode is given by:

$$\delta\nu = k\nu_0 \tag{12}$$

where:

$$\nu_0 = \frac{c}{2L}\frac{1}{\pi}\mathrm{acos}\sqrt{g_{\mathrm{IM}}g_{\mathrm{EM}}} \tag{13}$$

where L is the cavity length, g_{XX}, the g-factor of the input and end mirror as defined by $g_{\mathrm{XX}} = (1 - L/\mathrm{RoC_{XX}})$ with $\mathrm{RoC_{IM}}$ and $\mathrm{RoC_{EM}}$ are the Radius of Curvature of the input mirror and end mirror of the cavity, respectively. To be noted the g-factor of the arm cavity is given by the product $g_{\mathrm{IM}}g_{\mathrm{EM}}$ and is around 0.87 in the case of the Virgo arm cavities with the nominal RoC.

The distance between different modes normalized to the FSR is referred as the mode spacing. For example, the mode spacing between the zero and the first order modes can be written as:

$$\Delta\nu_1 = \frac{1}{\pi}\mathrm{acos}\sqrt{g_{\mathrm{IM}}g_{\mathrm{EM}}} \tag{14}$$

From Figure 2, using Equation 1, we could get the precise position of each peak and calculate the distance $\delta\nu$ between different orders. In order to calculate the Radius of Curvature of both

mirrors, we use the arm length $L = 2999.8$ m and the RoC values listed in Table 1 as a starting point, assuming the measurement error of both mirrors is the same. To be noted, as we are measuring the g-factor of the arm cavity and not directly the one of each individual mirror, we can not determine unambiguously the RoC of the input and end mirrors.

Finesse

The finesse of a Fabry-Pérot cavity can be defined as the ratio between the FSR and the Full Width Half Maximum (FWHM) of the TEM00 peak:

$$\mathcal{F} = \frac{f_{\mathrm{FSR}}}{f_{\mathrm{FWHM}}} \tag{15}$$

The finesse can be estimated using both the slow scans of the FSR and the fast swing of the cavity. Using the slow FSR scan performed with the ALS, both the f_{FSR} and the f_{FWHM} can be precisely measured and fit with a simple Airy function. We can directly use Equation 15 to calculate the finesse.

Using the ringing effect caused by the fast swing of the cavity mirror, the storage time of the cavity can be estimated from Equation 2, then finesse can be calculated using Equation 5.Statistically, higher speed induces more ringings, giving a more precise estimation on the finesse.

The finesse of the Fabry-Pérot cavity is determined by the reflectivity of the input and end mirrors, mathematically defined as:

$$\mathcal{F} = \frac{\pi\sqrt{r_{\mathrm{in}} r_{\mathrm{end}}}}{1 - r_{\mathrm{in}} r_{\mathrm{end}}} \tag{16}$$

where r_{in} and r_{end} are the amplitude reflectivity of the HR side of the input and end mirrors. In the Advanced Virgo Plus detector, manufacturing reasons have led to an asymmetry in the finesse between the two arms, significantly affecting the detector's Binary Neutron Star (BNS) range [18]. Therefore, it is crucial to correct this asymmetry. The input mirrors of the Advanced Virgo Plus interferometer have parallel surfaces, creating an etalon within the substrate. The optical path length of this etalon causes a modification on the transmissivity on the input mirror, consequentially changing the Finesse of the Fabry-Pérot cavity. The optical length inside the input mirror substrates can be controlled by adjusting temperature of the mirror itself, since it depends on the thermal expansion coefficient of the mirror material.

3.1.2. Reflected power comparison of lock/unlock states of the cavity

Among the multiple ways to define the round trip loss, if we consider the energy conservation principle, the loss is [19]:

$$\Lambda_{rt} = \frac{P_{\mathrm{in}} - P_{\mathrm{ref}} - P_{\mathrm{trans}}}{P_{\mathrm{circ}}} \tag{17}$$

where P_{in}, P_{ref}, P_{trans}, P_{circ} are, respectively, the input, reflected, transmitted and circulating power of the Fabry-Pérot cavity. Loss could be caused by different reasons, such as absorption in substrates and coatings or clipping, which could be due to a beam size larger than the mirror numerical aperture, or scattering from mirror surface defects. Measuring the RTL is needed to confirm that the quality of the optics is within the requirements. Moreover, it is also crucial to optimize the control of the interferometer, since loss could lead to smaller control signals and recycling gain. Furthermore, the performance of the squeezing can be largely affected by the loss level, higher loss means higher squeezing degradation and, as a consequence, less quantum noise reduction.

As mentioned in [20], we can assume the loss as an increase of the end mirror transmission. Therefore, we can estimate it from the reflectivity of the Fabry-Pérot cavity. In the case of a perfect cavity, without any loss and the end mirror perfectly reflective, all the power must be

reflected back from the cavity. Therefore, in this case, with the cavity locked or unlocked, the reflectivity (in power) of the cavity is always 1. As soon as small optical losses are introduced, the reflected power decreases linearly when the cavity is locked. So to estimate the RTL, we make a relative measurement looking at the reflected power (P_{ref}) with the same photodiode when the cavity is unlocked and locked. When the cavity is unlocked, the reflected power is equal to the incident power ($P_{\mathrm{ref}} = P_{\mathrm{in}}$), which is assumed to be also the reflected power when there is no loss in the locked cavity and the end mirror is perfectly reflective. Then, we lock the cavity and the reflected power decreases, the drop in power is directly related to the RTL. In this condition, we define $P_{\mathrm{ref}} = P_{\mathrm{lock}}$. Since it is a relative measurement, we do not need to know the optical losses between the cavity and the photodiode used for measurement, that is the strong advantage of this technique.

We first estimate the end reflectivity as:

$$\begin{aligned} r_{\mathrm{end}} &= \sqrt{1 - T_{\mathrm{end}} - \Lambda_{\mathrm{rt}}} \\ &\simeq \sqrt{1 - \Lambda_{\mathrm{rt}}} \end{aligned} \tag{18}$$

where r_{end} and T_{end} are the amplitude reflectivity and the power transmisivity of the end mirror. Then we could express the cavity reflectivity when it is locked as:

$$\begin{aligned} R_{\mathrm{cav}} &= \left[\frac{r_{\mathrm{in}} - r_{\mathrm{end}}}{1 - r_{\mathrm{in}} r_{\mathrm{end}}} \right]^2 \\ &\simeq \left[\frac{r_{\mathrm{in}} - \sqrt{1 - \Lambda_{\mathrm{rt}}}}{1 - r_{\mathrm{in}} \sqrt{1 - \Lambda_{\mathrm{rt}}}} \right]^2 \end{aligned} \tag{19}$$

Considering a locked cavity, we can write $P_{\mathrm{lock}} = P_{\mathrm{in}} \cdot R_{\mathrm{cav}}$ and, combining with Equation 19, we can express the round trip loss as:

$$\Lambda_{\mathrm{rt}} = \frac{T_{\mathrm{in}}}{2} \frac{1 - \frac{P_{\mathrm{lock}}}{P_{\mathrm{in}}}}{1 + \frac{P_{\mathrm{lock}}}{P_{\mathrm{in}}}} \tag{20}$$

P_{lock} and P_{in} can be acquired from both B4 and B1p PDs for the estimation of the round trip loss. This technique has been successfully used in the past to measure round trip losses in single Fabry-Pérot cavities [21], and more recently, also to characterize RTL in Virgo filter cavity, as a function of the beam position on the mirrors [22]. However, in a complex system as a gravitational wave detector, spurious beams also reach the PDs leading to unreliable results. An alternative way to estimate the round trip loss is through the recycling gain, as mentioned in the Section 3.2.1.

3.2. Recycling cavities

In addition to the arm cavities, we are also interested in the optical parameters of the recycling cavities, including the power recycling cavity length, the recycling gain of the carrier and sidebands, the arm circulating power and the contrast defect.

3.2.1. Carrier recycling gain

The optical gain of the PRC is called the recycling gain and is defined as follow when the interferometer is controlled in the dark fringe working point:

$$G_{\mathrm{PR}} = \left(\frac{t_{\mathrm{PR}}}{1 - r_{\mathrm{PR}} \cdot r_{\mathrm{FP}}} \right)^2 \tag{21}$$

where r_{PR} and t_{PR} are the amplitude reflectivity and transmissivity of the PR mirror and r_{FP} is the amplitude reflectivity of the Fabry-Pérot arm cavity, which can be expressed as:

$$r_{FP} = 1 - G_{FP} * \Lambda_{rt} \tag{22}$$

where $G_{FP} \simeq 286$ is the gain of the Fabry-Pérot cavity of AdV+ and Λ_{rt} is the round trip loss defined in Equation 20. The recycling gain of the PRC can be estimated using the DC power measured by the B7 or B8 photodiodes in transmission of two arm cavities in two different interferometer configurations. The first one is when only the Fabry-Pérot arm cavities are locked, and the second one is when the interferometer is fully locked. For example, if we consider the B7 photodiode, in the first working condition, the power measured can be written as:

$$P_{B7}^{FP} = P_{in} * T_{PR} * T_{BS} * G_{FP} * T_{NEM} \tag{23}$$

where P_{in} is the input power of the interferometer, T_{PR} is the power transmissivity of the PRM, T_{BS} is the power transmissivity of the BS, G_{FP} is the gain of the Fabry-Pérot arm cavity, and T_{NEM} is the power transmissivity of the North end mirror. On the other hand, the power measured by the B7 photodiode when the interferometer is fully locked can be expressed as:

$$P_{B7}^{DRFPMI} = P_{in} * G_{PR} * T_{BS} * G_{FP} * T_{NEM} \tag{24}$$

Combining Equations 23 and 24, the recycling gain is:

$$G_{PR} = T_{PR} * \frac{P_{B7}^{DRFPMI}}{P_{B7}^{FP}} \tag{25}$$

where the value of T_{PR} is given in Table 1.
Using the measured carrier recycling gain, together with Equation 22 and 21, the round trip loss of the arm cavities can be estimated.
From the recycling gain, another parameter which could also be estimated is the circulating power inside the arm cavities, defined as:

$$P_{circ} = \frac{1}{2} * P_{in} * G_{PR} * G_{FP} \tag{26}$$

3.2.2. Sideband recycling gain

To measure the gain of the sidebands, it is essential to obtain a power measurement independent of the carrier field. This is achieved using the phase camera, which can separately and simultaneously measure the powers of the carrier and sidebands. In order to compute the sideband gain, the measurement must be normalized against a simpler reference configuration, where the power can be easily estimated. This reference is provided by what we call "single bounce configuration" described in the next section.

To avoid multiple bounces in the recycling cavities, the single bounce configuration is often set during the phase of commissioning. The single bounce condition for one arm cavity is created by misaligning its end mirror, while the input and end mirrors of the other arm cavity are completely misaligned. Power and signal recycling mirrors are also misaligned. In this state, the B1p and B4 sensors only measure the reflection from one input mirror. This setup accounts for losses introduced by all auxiliary optics from the input mirror to the sensors, and serves as a baseline for characterizing the full interferometer.

The phase cameras once calibrated are a unique tool for estimating various optical parameters of the interferometer, such as the sideband gain and contrast defect (CD). The intensity of the different fields captured by the phase camera results from the beating signal between the

interferometer beam (comprising the carrier, 6 MHz, and 56 MHz sidebands) and a reference beam, which is a pickoff of the Virgo main laser offset in frequency. This beating signal is then demodulated at different frequencies to retrieve information about the individual components. Comparing the sideband power between the single bounce and the fully locked configurations, the sideband gain can be estimated. The sideband reference power measured by the B4 phase camera in the single bounce configuration can be written as:

$$P_{\mathrm{B4}}^{\mathrm{ref}} = P_{\mathrm{in}} * T_{\mathrm{PR}} * T_{\mathrm{BS}} * R_{\mathrm{in}} * T_{\mathrm{BS}} \tag{27}$$

where T_{BS} is the power transmissivity of the beam splitter, and R_{in} is the power reflectivity of the input mirror HR surface. When the interferometer is fully locked, the sideband power measured by B4 phase camera can be expressed as:

$$P_{\mathrm{B4}}^{\mathrm{DRFPMI}} = P_{\mathrm{in}} * G_{\mathrm{SB}} \tag{28}$$

where G_{SB} is the sideband gain. Combining Equations 27 and 28, the recycling gain for the sidebands is:

$$G_{\mathrm{SB}} = T_{\mathrm{PR}} * T_{\mathrm{BS}}^2 * R_{\mathrm{in}} * \frac{P_{\mathrm{B4}}^{\mathrm{DRFPMI}}}{P_{\mathrm{B4}}^{\mathrm{ref}}} \tag{29}$$

The theoretical values of the gain of the sidebands can be calculated as the carrier one using Equation 21, with the $r_{\mathrm{FP}} = 1$ as the sidebdans are not resonant in the arms. The formula is correct for the 6 MHz sidebands, which are almost on the dark fringe and not impacted by the presence of SRM. For the 56 MHz sidebands, due to the Michelson length asymmetry explained in Section 3.5 and since they are also resonant inside the SRC, although it is possible to derive an analytical model, the calculation of $r_{\mathrm{FP}}^{56\,\mathrm{MHz}}$ is more complex and the values of the gain can be easier estimated through simulations.

3.3. Contrast defect

The contrast defect of an interferometer is used to characterize the amount of excess light reaching the dark port. It can be expressed as the ratio between the power of the excess light and the circulating power inside the interferometer. Mathematically, it can be written as:

$$\mathrm{CD} = 2 * \frac{P_{\mathrm{min}}}{P_{\mathrm{max}}} \tag{30}$$

where P_{min} and P_{max} are the minimum and maximum powers measured at the output of the interferometer, and correspond to the power measured by the B1p and B4 sensors. Using the power from the B1p and B4 phase cameras when the interferometer is in single bounce and in the fully locked states, we can deduct the contrast defect expression of the interferometer before the OMC as:

$$CD = 2 * T_{\mathrm{SR}} * \frac{\frac{P_{\mathrm{B1p}}^{\mathrm{DRFPMI}}}{P_{\mathrm{B1p}}^{\mathrm{ref}}}}{\frac{P_{\mathrm{B4}}^{\mathrm{DRFPMI}}}{P_{\mathrm{B4}}^{\mathrm{ref}}}} \tag{31}$$

where T_{SR} is the power transmissivity of the signal recycling mirror.

3.4. Modulation depth of the sidebands

The modulation depth of the 56 MHz and 6 MHz sidebands is estimated by the relative power between the sidebands and the carrier, defined as:

$$m = \sqrt{\frac{2 * P_{\mathrm{SB}}}{P_{\mathrm{car}}}} \tag{32}$$

where P_{SB} and P_{car} are the total powers of the sidebands and of the carrier. These powers can be estimated through data collected using two different approaches: the slow FSR scans and the phase camera in the single bounce configuration:

- From the slow FSR scans, as the one shown in Figure 2, the peak height of the 56 MHz and 6 MHz sidebands can be estimated using Equation 1.
- The power of the sidebands can be acquired independently from the phase camera used in the single bounce configuration. The result obtained acquiring the modulation depth from the phase camera data can be used to confirm the estimation made analyzing the data from the scan.

3.4.1. Power recycling cavity length

During the interferometer steady-state operation, the carrier and the sidebands at 6 MHz and at 56 MHz have to resonate in the PRC. While the carrier resonance is guranteed by changing the microscopic length of the PRC, using a Pound-Drever-Hall (PDH) locking error signal obtained by beating the carrier with the anti-resonant sidebands at 8 MHz, the resonance condition of the sidebands depends on the macroscopic length of the cavity. The sideband resonance condition can be written as:

$$2\frac{2\pi f}{c}l_{PR} + \pi = 2N\pi \tag{33}$$

where the additional π picked up after a round trip is due to the anti-resonant sidebands in the arms, and N is an integer. The relation between the cavity length and the resonance frequency f can be defined as:

$$f = (2N-1)\frac{c}{4l_{PR}} \tag{34}$$

If the macroscopic cavity length is such that the sidebands are resonant in the PRC, the optimal demodulation phase of the PDH signal will have a difference of 180° between the carrier and the sidebands. A change in the PRC length moves the sidebands away from the resonance resulting in a shift of the optimal demodulation phase difference away from 180°. The PRC length change Δl_{PR} can be measured by checking how much the optimal PDH demodulation phase shift deviates from the expected 180° when optimizing the demodulation frequency to lock the PRC purely on the resonance of the carrier or of the sidebands. The relation between the phase shift $\delta\phi_{PDH}$ and the length mistuning depends on the PRC finesse $\mathcal{F}_{PR}$ as:

$$\Delta l_{PR} = \frac{c}{4f\pi}\frac{2\mathcal{F}_{PR}}{\pi}\frac{\delta\phi_{PDH}}{180} \tag{35}$$

The measurement has been performed using the 6MHz RF signal on B2 photodiode, with only the central interferometer locked.

3.5. Michelson arm length (Schnupp) asymmetry

A macroscopic asymmetry in the lengths of the arms of the short Michelson interferometer, known as Schnupp asymmetry, is required to transmit part of the sidebands toward the dark port where they are use for generating control error signals. The beam reflected by the two arm cavities travel different distances resulting in a relative phase shift, which depends on the Schnupp asymmetry δl_{MICH} and on the modulation frequency f_i (i indicating which modulation frequency) as: $\delta\phi = 2\delta l_{MICH}\frac{2\pi f_i}{c}$ for one round trip. This can be measured by locking one arm at a time, and recording the optimal demodulation phase for each cavity. From the difference in the optimal demodulation phase of the two arms we can directly compute the Schnupp asimmetry as:

$$\delta l_{MICH} = \delta\phi\frac{c}{4\pi f_i} \tag{36}$$

The measurement has been performed using the 6MHz RF signal on B4 photodiode.

4. Arm cavity optical parameter measurements

All the measurements were performed using the arm cavity slow FSR scan method during the commissioning activities needed to find the best working point of the interferometer in view of O4. Therefore, they have been performed with different input powers and TCS tunings, as described in section 2.2. The main results presented in the following sections have been obtained with the final configuration of the interferometer chosen for O4, meaning that the input power is 17 W, and they are compared with the values obtained in different working conditions. The speed of the scan is about 1 kHz/s, while the cavity FSR is about 50 kHz. Each group of measurements consists of four full FSRs, obtained by scanning the frequency with a ramp. They have been repeated for some minutes to give enough statistic for more accurate parameter estimations.

4.1. Arm cavity lengths

From the measurement of the FSR scan as illustrated by the figure 2, the value d_{SB} (position of the SBs in the FSR, see Equation 1) can be derived using the 56 MHz sidebands. We found d_{SB} equals to 0.4536 ± 0.0002 and 0.4416 ± 0.0002, respectively for the NA and WA. The corresponding arm lengths are 2999.8203 ± 0.0004 m and 2999.7884 ± 0.0005 m, deducted from f_{FSR}. The difference between arm lengths $L_N - LW$ is 0.0319 ± 0.0006,m. It was also confirmed in the simulation made with both OSCAR [23] and Finesse [24] that the NA is about 3 cm long than the WA.

4.2. Finesse

The design finesse value of the arm cavities can be calculated using Equation 16. The nominal value for the Advanced Virgo Plus cavities is about 450. Considering the etalon effect [25], the finesse of the North arm could change between 448 and 458, while the one of the West arm varies between 447 and 461.
From the slow scan, the finesse was estimated through Equation 15. Using the data of 6 scans, the values obtained for the estimations of the finesse of the cavities are 459.51 ± 6.19 for NA and 454.73 ± 8.14 for WA.
The finesse has been estimated also using the ringing effect, with Equation 5. Figure 5 shows the histograms of the finesse estimated using the ringing. The results are 452 ± 4 for NA and 448 ± 7 for WA, slightly different compared with the ones obtained using the slow scan. This could be due to different etalon conditions of the input mirrors between the two finesse measurements.

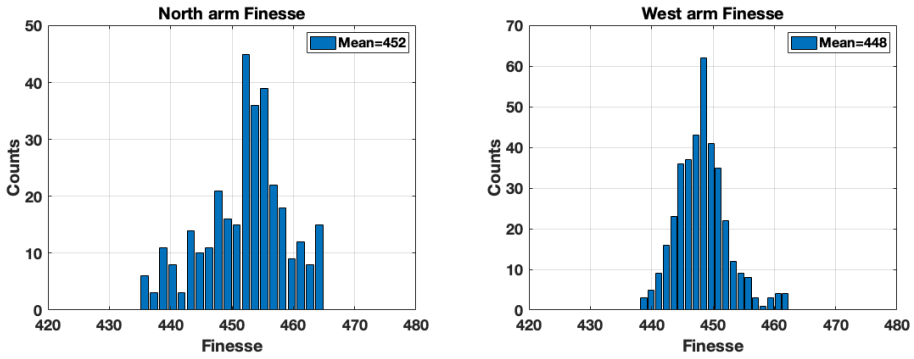

Fig. 5. Histograms of the estimated Finesse using the ringing effect.

4.3. Mode-matching

The values of the mode-matching of the beam into the Fabry-Pérot cavities are estimated through the relative peak height between the second-order mode and the fundamental mode, as described in section 3.1. For the cold cavities, the obtained results are 97.19 ± 0.15 % for NA and 98.93 ± 0.06 % for WA, respectively. For the hot cavities, the obtained values are 97.45 ± 0.04 % and 99.12 ± 0.01 %. The difference between the two arms could be caused by the slightly different RoCs of the mirrors, the different RoCs of the CPs and the independent tuning of the TCS actuators.

4.4. Radius of curvature

The radii of curvature of the cavity mirrors are estimated through Equation 14, using slow FSR scan and then measuring the distance between the second order modes and the fundamental one. Once normalised by the FSR, this value is directly related to the g-factor of the cavity. We choose to use the position of the second order modes in the FSR as it appears to be the most robust mode, insensitive to misalignment.

The same technique can also be used to estimate the g-factor of the arm cavities when the full power is circulating inside the interferometer. For that, we lock the interferometer for at least one hour and then on purpose unlock the arms and start the slow scan. For the final O4 configuration with 17 W of input power, the evolution of the g-factor for both cavities from hot to cold is shown in figure 6.

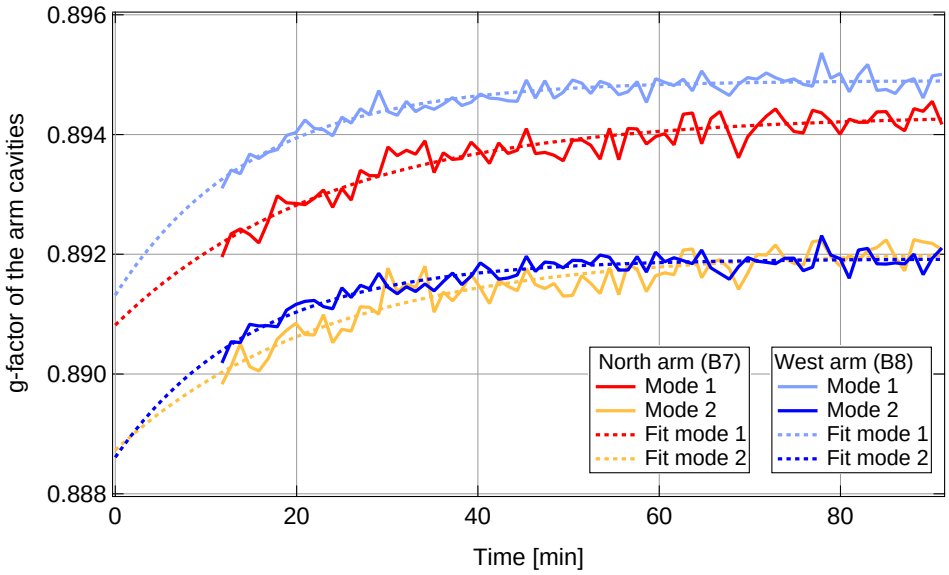

Fig. 6. Evolution of the g-factor of the arm cavities from hot to cold. This measurement is derived from the position of the second order modes inside the FSR. The position is fitted as 2 peaks per cavity to take into account the presence of astigmatism, usually visible on all the modes. So in total 4 curved are presented and fitted with a decay function (simple exponential).

For O4, the ring heaters around the end mirrors are switched on permanently to optimise the contrast defect, by comparing the g-factor of the cavity with the ring heater off and on, it is possible to estimate the change of RoC due to the action of the ring heater. Using the cold g-factor from the figure 6, with a ring heater power of 7.1 W for the North arm and 8.2 W for

the West one, it was found that the measured RoC changes are respectively about -24.6 ± 0.9 m and -27.3 ± 0.6 m for the end mirrors. To be noted that before the start O4, the ring heater were further tuned by 0.1 W but no FSR scan was done after.

The radii curvature of the mirrors in the hot cavity configuration were also estimated from Figure 6 for both cavities. The time $t = 0$ in the abscissa represents the moment of the unlock in the interferometer. Fitting the data with a decay function ($f(t) = a \times \exp(-bt) + c$) with the coefficients a, b and c, the g-facor in the hot cavity configuration can be estimated by $f(t = 0)$. The three coefficients represent: a, the change in the g-factor between the hot and the cold cavity configurations. b, the inverse of the time constant and, c, g-factor in the cold state. In Figure 6, the fits are shown in red and blue dashed lines for the North and West arms. 4 fits are done in total, 2 per arms one for each second order modes but the same time constant is used for a given arm.

Table 2. Fitted parameters from the evolution of the cavity g-factor with data from figure 6.

Mode	**a**$\times 1000$	**b** $\times 10000$	**c**
NA Mode 1	-3.5 ± 0.2	-7.0 ± 0.6	0.8943 ± 0.0001
NA Mode 2	-3.3 ± 0.2	-7.0 ± 0.6	0.8920 ± 0.0001
WA Mode 1	-3.6 ± 0.3	-10.9 ± 0.6	0.8949 ± 0.0001
WA Mode 2	-3.3 ± 0.2	-10.9 ± 0.6	0.8919 ± 0.0001

From the parameter a in table 2, it is obvious that the thermal effect is quite similar for both arms. Assuming the change in RoC distributes equally on the input and end mirrors (which is not rigrously true due to the difference in beam size), we can conclude the RoC change per mirror is about 1.5 ± 0.1 m for the North and West arms.

An overlapping double resonance peak was observed in some first higher-order modes during the scan, suggesting astigmatism, leading to different resonance conditions in 2 different directions. That is the reason why in the analysis of the cavities g-factor, 2 peaks are fitted for the second order mode. From the difference in the c parameters for the same arm, one can express the astigmatism as the difference of RoC in 2 different directions. Based on the value from the table 2, we found the RoC difference for North arm to be 1.8 ± 0.2 m and 2.4 ± 0.2 m for the West arm if we assume the astigmatism to be induced by one single mirror of the cavity.

To further investigate the level of astigmatism in each arm, angular misalignments were applied separately (and sequentially) to each degree of freedom of the cavity mirror while scanning the cavity. As the result we can excite only one first order mode for example the TEM10 as shown in figure 7. The resulting spacing for the first-order mode resonances TEM10 and TEM01 were computed. From this result, the difference of RoC between the 2 perpendicular directions is found to be 1.3 ± 0.7 m and 2.5 ± 0.6 m, respectively for the NA and WA arms. It should be noted that the astigmatism is not necessary along the direction of misalignment of the mirrors and so the analysis could be more complex but the values are compatible with the analysis with the second order modes.

4.5. Round trip losses

Using Equation 20, the round trip loss of a Fabry-Pérot cavity can be calculated comparing the power acquired by the photodiodes in reflection, while the cavity is locked and unlocked. In the case of AdV+, the usual photodiodes used to collect the data are the B4 or the B1p ones. The data is acquired for one cavity at a time, with cavity locking/unlocking periods of 30 s. The

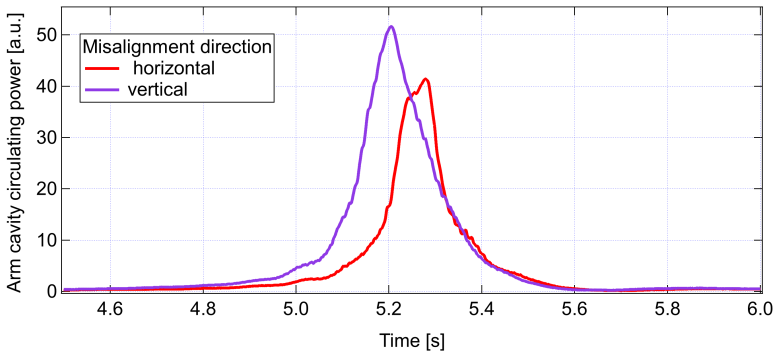

Fig. 7. Zoom on the resonances of the first order mode during a FSR scan with the arm cavity misaligned in the horizontal and vertical directions. The shift in the resonances of the mode TEM 10 and 01 could be explained by the presence astigmatism in the arm cavity.

measurements are repeated few times to obtain some statistic. However, as mentioned in Section 3.1.2, the presence of different spurious beams when the cavity is locked and unlocked led to not reliable estimations of the round trip loss. In Figure 8, examples of such measurements for cold cavities are shown using two B4 photodiodes. The estimated RTL is 100 ± 10 ppm for both the NA and the WA. The cold arm cavity RTL was measured to be 55 ppm [26]. Compared to simulations based on the characterization of individual mirrors, including low-frequency surface aberrations and scatterometer data, an additional loss of around 10 ppm per mirror was observed inside the interferometer. In the next section, the results obtained for the estimation of the RTL starting from the power recycling gain will be presented.

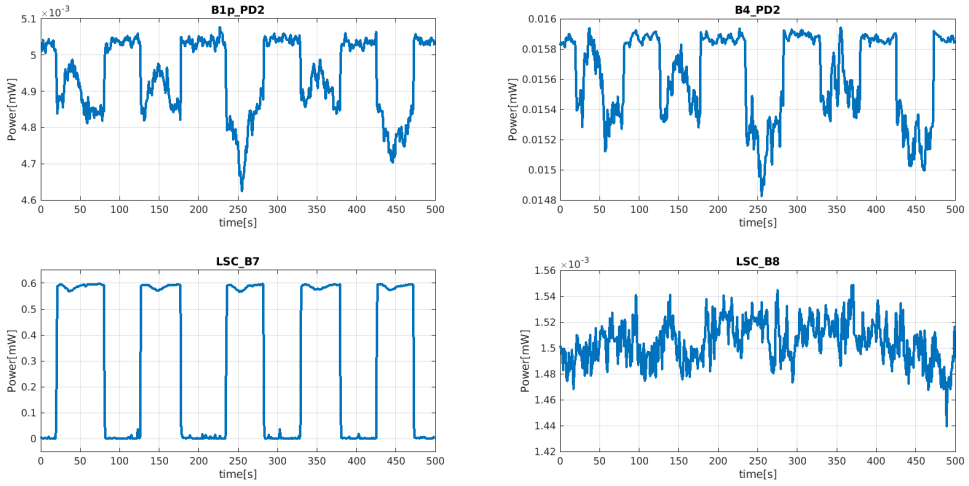

Fig. 8. The two top plots show an example of the RTL measurement of the North arm, with 17 W of input power, using two different photodiodes: one is installed at the dark port along the B1p path, and the other one is on the B4 path, a pick-off extracted in the PRC. The two bottom two plots show the transmissions of the NA and WA, respectively acquired by the B7 and B8 photodiodes. The two different phases of the measurement correspond to lock and unlock of the NA cavity, while the WA cavity is completely misaligned.

5. Recycling cavity optical parameter measurements

5.1. Power recycling cavity length

Based on the estimation from the analytical model and the simulations, the optimal power recycling cavity length l_{PR} should be around 12.073 m. Applying Equation 35, with the 56 MHz sidebands, a demodulation phase shift of 0.4 rad was measured, which corresponds to about 3.3 ± 0.5 mm of length mistuning from the optimal l_{PR} without a definite sign.

5.2. Michelson length (Schnupp) asymmetry

By locking the cavities formed by PR and NI or PR and WI, one at a time, and optimizing the demodulation phases with a precision of 0.1°, the asymmetry in the Michelson arm length, i.e. the Schnupp asymmetry, was measured to be 22.9 ± 0.4 cm.

5.3. Carrier gain

The recycling gain of the carrier has been estimated through the Equation 25 at different input powers of the interferometer during the whole commissioning period. For each input power, the power transmitted by NA has been measured by the B7 photodiode in two different states of the interferometer: the first one is when only the arm cavities are locked and the second one is when the full interferometer is locked. The results are shown in the left plot of Figure 9. We can observe that increasing the input power, the recycling gain is decreasing due to partially uncompensated thermal aberration. The same trend has been observed also in LIGO [27]. The right plot of Figure 9 shows the circulating power in the arms as a function of the input power. One thing to be noted is that the North end mirror of the AdV+ detector was replaced in June 2023. The blue and red dots in the figure represent the measurements done before and after the mirror replacement. A slight increase in the recycling gain was measured after changing the North end mirror. From the recycling gain, we also estimated the round trip loss of the arm cavities listed in Table 4, assuming all the gain reduction are induced only by the round trip loss.

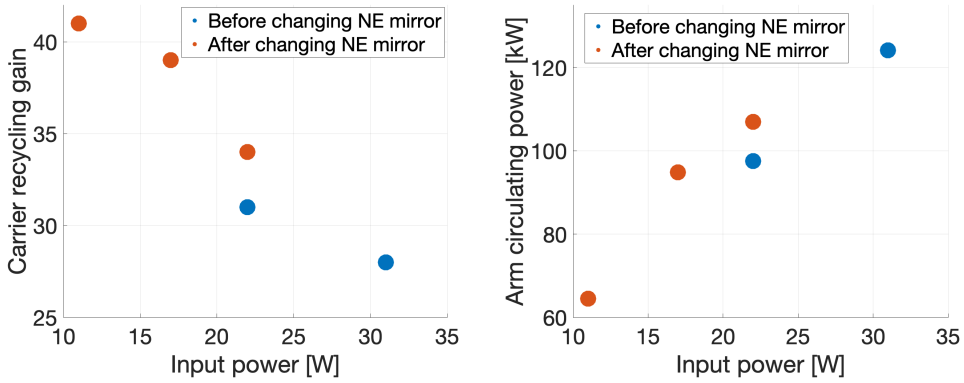

Fig. 9. Left plot: Measured recycling gain of the carrier for different input powers of the interferometer. Right plot: Arm circulating power inside the interferometer for different input powers.

5.4. Sidebands gain

The recycling gain of the sidebands has been calculated through Equation 29 with different input powers. Assuming the transmissivity of the beam splitter $T_{BS} = 0.5$, each sideband power has been acquired by the B4 phase camera in two interferometer states: the first one is the single bounce configuration, to have a reference power, while the second one is with the interferometer fully locked. For the second state, the measurements were taken both right after the lock (cold state) and one hour after the lock (hot/steady state). In Table 3, the values estimated for the gains of the 56 MHz and 6 MHz sidebands for the cold and hot cavity configurations are listed, compared to the theoretical ones. These values are the averages between the values of the upper and the lower sidebands. The upper and lower sidebands were well balanced for the 6 MHz, for which the difference was less than 1.6 %. On the other hand, for 56 MHz, the difference was around 11 % . For the final O4 configuration, the recycling gain of the 6 MHz sideband was 24 ± 0.7, while the one of the the 56 MHz sideband was 17 ± 0.9 for for the hot cavity configuration.

Table 3. Comparison of the recycling gain for the carrier, 6 MHz sidebands and 56 MHz sidebands among the theoretical values, cold (right after the lock of the full interferometer) and hot (1 h after the lock of the full interferometer) states for 17 W of input power. The theoretical carrier and sidebands recycling gain value is given for a perfect interferometer with the unique defect of 60 ppm of round trip loss in the arm cavities

	G_{car}	$G_{6\,MHz}$	$G_{56\,MHz}$
Theoretical	42	72	53
Cold state	42	48	26
Hot state	39	24	17

5.5. Arm circulating power estimation

Using the recycling gain of the carrier estimated in Section 5.3 and Equation 26, we calculated the circulating powers in the arm cavities for different interferometer input powers. The results are shown on the right plot of Figure 9. For the final O4 configuration, the circulating power is 96 ± 1 kW.

5.6. Contrast defect

The contrast defects for different interferometer input powers have been estimated through Equation 31. The power of the carrier measured by the B1p and B4 phase cameras in two different interferometer states are used: the first state is the single bounce configuration, while the second state refers to the fully locked interferometer with the signal recycling mirror misaligned by approximately 2 μrad in the vertical direction, resulting in a 75% reduction in the contrast defect. For the final O4 configuration, the optimized contrast defect of the interferometer is $(2.86 \pm 0.24) \times 10^{-4}$ before the OMC, and 6×10^{-8} after the OMC. Although not the focus of the article, optical simulations of the full interferometer were conducted, including wavefront distortions from the cold mirrors (assuming perfect TCS compensation of the thermal effects). The results showed that the measured contrast defect after the SRM was twice higher than the estimate provided by the simulations. More accurate simulations would require to include all the wavefront distortions including the effects of the optical absorption and the TCS corrections.

5.7. Summary

In Table 4, we summarize all the parameters mentioned in Section 5 that have been measured with different interferometer input powers during the commissioning period. Except the measurements of 31 W of input power, all the other measurements were performed after the replacement of the North end mirror. Moreover, the contrast defects for all the input power except 31 W were measured with misaligned SRM.

Table 4. Summary of all the mentioned parameters measured with different input powers during the O4 commissioning period. Except for 31 W of input power, all the results are given with SR misaligned.

P_{in} (W)	G_{PR}	G_{SB} 6 MHz	G_{SB} 56 MHz	P_{circ} (kW)	CD	RTL (ppm)
11	41	29	20	65	4.2×10^{-4}	61
17	39	24	17	96	2.9×10^{-4}	68
22	34	22	17	108	7.3×10^{-4}	85
31	28	27	18	125	1.8×10^{-3}	112

6. Modulation depth measurements

The modulation depth of the sidebands was estimated through two different measurements, as mentioned in Section 3.4. The obtained results are summarized in Table 5 for the 56 MHz and 6 MHz upper and lower sidebands. For the phase camera method, data were acquired using both the B1p and B4 sensors. The estimated values of the modulation depth obtained using the two methods listed in the table are in a good agreement.

Table 5. Modulation depth of the 56 MHz and 6 MHz upper and lower sidebands estimated analysing the data obtained both through the FSR scan, and form the B1p and the B4 phase cameras used in the single bounce configuration. The results from the different measurements are in good agreement.

	FSR scan	B1p phase camera	B4 phase camera
56 MHz upper sideband	0.189	0.193	0.197
56 MHz lower sideband	0.183	0.193	0.197
6 MHz upper sideband	0.201	0.206	0.210
6 MHz lower sideband	0.202	0.206	0.210

7. Conclusion

In this paper, we describe the methods adopted for the characterization of the optical parameters of the AdV+ detector during the commissioning phase in view of the O4 Observing Run. In particular, for the characterization of the Fabry-Pérot arm cavities, the implementation of an Aunxiliary Laser System provided the possibility of performing slow scans of the free spectral range. Using this method we could estimate the arm cavity length, the mode-matching and alignment between the input beam and the arm cavities, the radius of curvature of the cavity mirrors and the cavity finesse. All the measurements needed for the characterization could be

performed with different configurations of the interferometer and various tunings of the Thermal Compensation System. Also the estimation of some parameters of the recycling cavities was performed in different inteferometer configurations. Among these parameters we could estimate the recycling gain for both the carrier and the sidebands, the power circulating in the arm cavities and the contrast defect. In particular, in this papers the optical parameters measured in the final Advanced Virgo Plus configuration optimized for O4 have been presented. These measurements triggered a simulation work for a more deeper understanding of the detector, which is out of the scope of this paper and will be detailed in another article.

Acknowledgments

The authors gratefully acknowledge the Italian Istituto Nazionale di Fisica Nucleare (INFN), the French Centre National de la Recherche Scientifique (CNRS) and the Netherlands Organization for Scientific Research (NWO), for the construction and operation of the Virgo detector and the creation and support of the EGO consortium. The authors also gratefully acknowledge research support from these agencies as well as by the Spanish Agencia Estatal de Investigación, the Consellera d'Innovació, Universitats, Ciència i Societat Digital de la Generalitat Valenciana and the CERCA Programme Generalitat de Catalunya, Spain, the National Science Centre of Poland and the European Union – European Regional Development Fund; Foundation for Polish Science (FNP), the Polish Minister of Science, the Hungarian Scientific Research Fund (OTKA), the French Lyon Institute of Origins (LIO), the Belgian Fonds de la Recherche Scientifique (FRS-FNRS), Actions de Recherche Concertées (ARC) and Fonds Wetenschappelijk Onderzoek – Vlaanderen (FWO), Belgium, the Aristotle University of Thessaloniki (AUTH), the European Commission. The authors gratefully acknowledge the support of the NSF, STFC, INFN, CNRS and Nikhef for provision of computational resources. The authors would like to extend special thanks to the control room operators, whose efforts made this work possible: Andrea Magazzu, Beatrice Montanari, Fabio Gherardini, Francesco Berni, Gianmatteo Sposito, Lorenzo Irace and Nicola Menzione.

References

1. B. P. Abbott *et al.*, "LIGO: the laser interferometer gravitational-wave observatory," Reports on Prog. Phys. **72**, 076901 (2009).
2. F. Acernese *et al.*, "Advanced Virgo: a second-generation interferometric gravitational wave detector," Class. Quantum Gravity **32**, 024001 (2015).
3. T. V. Collaboration, "Advanced virgo plus phase i design report," https://tds.virgo-gw.eu/?content=3&r=20962.
4. T. V. Collaboration, "Advanced virgo plus phase ii design report," https://tds.virgo-gw.eu/?content=3&r=20962.
5. B. P. Abbott, R. Abbott, T. D. Abbott, *et al.*, "Prospects for observing and localizing gravitational-wave transients with advanced ligo, advanced virgo and kagra," Living Rev. Relativ. **23** (2020).
6. M. Ando, K. Arai, K. Kawabe, and K. Tsubono, "Demonstration of power recycling on a fabry-perot-type prototype gravitational wave detector," Phys. Lett. A **248**, 145–150 (1998).
7. E. D. Black, "An introduction to Pound–Drever–Hall laser frequency stabilization," Am. J. Phys. **69**, 79–87 (2001).
8. http://lma.in2p3.fr/Lmagb.htm.
9. L. Aiello, E. Cesarini, V. Fafone, *et al.*, "Thermal compensation system in advanced and third generation gravitational wave interferometric detectors," J. Physics: Conf. Ser. **1226**, 012019 (2019).
10. A. F. Brooks, T.-L. Kelly, P. J. Veitch, and J. Munch, "Ultra-sensitive wavefront measurement using a hartmann sensor," Opt. Express **15**, 10370–10375 (2007).
11. I. Nardecchia, Y. Minenkov, M. Lorenzini, *et al.*, "Optimized radius of curvature tuning for the virgo core optics," Class. Quantum Gravity **40**, 055004 (2023).
12. T. Accadia, F. Acernese, M. Agathos, *et al.*, "Central heating radius of curvature correction (chrocc) for use in large scale gravitational wave interferometers," Class. Quantum Gravity **30**, 055017 (2013).
13. I. Khan, E. Genin, V. Fafone, *et al.*, "Auxiliary lasers for advanced virgo gravitational wave detector using single pass second harmonic generation in periodically poled lithium niobate crystal," J. Physics: Conf. Ser. **1548**, 012025 (2020).

14. C. De Rossi, J. Brooks, J. Casanueva Diaz, *et al.*, "Development of a frequency tunable green laser source for advanced virgo+ gravitational waves detector," Galaxies **8** (2020).
15. J. Poirson, F. Bretenaker, M. Vallet, and A. L. Floch, "Analytical and experimental study of ringing effects in a fabry–perot cavity. application to the measurement of high finesses," J. Opt. Soc. Am. B **14**, 2811–2817 (1997).
16. M. Rakhmanov, "Dynamics of laser interferometric gravitational wave detectors," Phd thesis, California Institute of Technology (2000).
17. D. Z. Anderson, "Alignment of resonant optical cavities," Appl. optics **23**, 2944–2949 (1984).
18. A. Chiummo and G. Vajente, "Itf asymmetries and coupling of laser technical noises," https://tds.virgo-gw.eu/?content=3&r=9206.
19. R. B. Jerome Degallaix, Massimo Galimberti and Q. Benoit, "Defining the arm cavity loss for advanced virgo," Virgo internal note:VIR-706A-10.
20. M. L. F. Bondu and J.-Y. Vinet, "From mirror maps to tem00 model: evaluation of effective losses," https://tds.virgo-gw.eu/?content=3&r=1940.
21. E. Capocasa, Y. Guo, M. Eisenmann, *et al.*, "Measurement of optical losses in a high-finesse 300 m filter cavity for broadband quantum noise reduction in gravitational-wave detectors," Phys. Rev. D **98**, 022010 (2018).
22. Y. Zhao, M. Vardaro, E. Capocasa, *et al.*, "Optical losses as a function of beam position on the mirrors in a 285-m suspended fabry-perot cavity," Phys. Rev. Appl. **22**, 054040 (2024).
23. https://nl.mathworks.com/matlabcentral/fileexchange/20607-oscar.
24. https://finesse.ifosim.org.
25. J. Brooks, M. Mantovani, A. Allocca, *et al.*, "Temperature control for an intra-mirror etalon in interferometric gravitational wave detector fabry–perot cavities," Galaxies **8**, 80 (2020).
26. J. Degallaix, C. Michel, B. Sassolas, *et al.*, "Large and extremely low loss: the unique challenges of gravitational wave mirrors," J. Opt. Soc. Am. A **36**, C85–C94 (2019).
27. A. F. Brooks, G. Vajente, H. Yamamoto, *et al.*, "Point absorbers in advanced ligo." Appl. optics **60 13**, 4047–4063 (2021).